Executive Summary

Focal Plane Assembly Technology Development for SPICA/SAFARI

Under GSTP contract

Prepared by:

SRON Netherlands Institute for Space Research

Table of contents

Abbreviations and acronyms

Item	Meaning
CTE	Coefficient of thermal expansion
FDM	Frequency division multiplexing
FEM	Finite element modelling
FPA	Focal plane assembly
FTS	Fourier transform spectrometer
IR	Infrared
LHe	Liquid helium
LN2	Liquid nitrogen
SQUID	Superconducting quantum interference device
TES	Transition edge sensor
T_c	Superconducting transition temperature

Applicable Documents

[AD#]	Doc. Reference	Issue	Title
[AD1]	ESA Contract No. 4000110555	1	Focal Plane Assembly Technology Development for SPICA/SAFARI

Reference Documents

[RD#]	Doc. Reference	Issue	Title
[RD1]	TEC-MME/2013/61	1	Statement of Work: Focal Plane Assembly Technology Development for SPICA/SAFARI
[RD2]	SRON-LEA-PR-13-001	1	"Focal Plane Assembly Technology Development for SPICA/SAFARI ", RFQ/3-14040/13/NL/PA
[RD3]	SRON-SAFARI-TN-2015-008	1	Summary report - FPA technology development for SPICA/SAFARI
[RD4]	SRON-SAFARI-TN-2015-010	1	Abstract - FPA technology development for SPICA/SAFARI
[RD5]	SRON-SAFARI-TN-2014-003	1	TN1.1 Demonstrate Nb on polyimide on silicon process
[RD6]	SRON-SAFARI-TN-2014-004	1	TN1.2 Demonstrate Nb on polyimide flex circuit process
[RD7]	SRON-SAFARI-TN-2014-005	1	TN1.3 Demonstrate superconducting coils in the flex circuit process
[RD8]	SRON-SAFARI-TN-2014-006	1	TN1.4 Demonstration of a “fixed” interconnect–to–LC Filter contact
[RD9]	SRON-SAFARI-TN-2014-007	1	TN1.5 Fabrication prototype chips for the 50 mK EM
[RD10]	SRON-SAFARI-TN-2015-007	1	TN1.6 Demonstration of an interconnect + LC filter assembly
[RD11]	SRON-SAFARI-TN-2014-008	1	TN2.1 Definition of B-shield EM test plan and conceptual design
[RD12]	SRON-SAFARI-TN-2014-009	3	TN2.2 Prototype shield measurement setup and results
[RD13]	SRON-SAFARI-TN-2014-010	1	TN2.3 B-shield EM detailed design, manufacturing and assembly
[RD14]	SRON-SAFARI-TN-2014-011	1	TN3.1 Conceptual design of 50mK electronics assembly & interconnect requirements
[RD15]	SRON-SAFARI-TN-2014-012	1	TN3.2 Preliminary design of interconnect assembly and tooling
[RD16]	SRON-SAFARI-TN-2014-013		TN3.3 Detailed design of 50 mK EM + assembly tooling
[RD17]	SRON-SAFARI-TN-2014-014		TN3.4 50 mK EM manufacturing, assembly & testing
[RD18]	SRON-SAFARI-TN-2015-001	1	TN4.1 B-shield EM functional- and baseline performance tests in EM configuration
[RD19]	SRON-SAFARI-TN-2015-002	1	TN4.2 Performance tests of alternative B-shield configurations
[RD20]	SRON-SAFARI-TN-2015-003	1	TN4.3 50mK EM thermal cycle and vibration test results
[RD21]	SRON-SAFARI-TN-2014-017	1	TN5.1 Analysis and conclusions from baseline B-shield shielding tests
[RD22]	SRON-SAFARI-TN-2015-005	2	TN5.2 Analysis and conclusions from WP1 to WP4
[RD23]	UTwente EMS report	October 7, 2014	Results of the zero field and field cooled measurements on the Nb shield and Nb and Cryoperm assembly

1 Document scope

The document summarizes the work performed and result achieved within the scope of the of an ESA GSTP contract "Focal Plane Assembly Technology Development for SPICA/SAFARI " ([AD1]), in accordance with ESA's Statement of Work ([RD1]) and SRON's proposal ([RD2]). Additional summaries can be found in:

- [RD3] - Summary report, Focal plane assembly technology development for SPICA/SAFARI
- [RD5]-[RD22] - Technical datapackage, FPA technology development for SPICA/SAFARI

2 Project introduction

Cryogenic instruments based on imaging arrays of superconducting Transition Edge Sensor (TES) detectors operating at very-low temperature are proposed or considerd for future high- and low-energy astrophysics space missions, including the X-IFU instrument for Athena and the SAFARI instrument for SPICA.

2-D arrays of 1000's of TES detectors at 50 mK enable high-sensitivity imaging with high optical efficiency and fast response. The detectors are operated using frequency division multiplexed SQUID amplifiers that offer the low input noise and input impedance required for TES readout, with a low power dissipation to fit within the limited cooling powers available at low temperatures. The TES detectors and their SQUID readout electronics are to be integrated inside Focal Plane Assemblies (FPAs) that isolate the detectors and their readout electronics at 50 mK from their environment. Fig. 2-1 shows a preliminary concept for one of the far-IR TES FPA's in SAFARI. A similar design concept is considered for the TES FPA in the X-IFU instrument.

This project has focussed on three enabling technologies for a TES FPA: a) magnetic shields to suppress spurious detector signals due to background magnetic fields; b) high-density flexible interconnects to connect a large-format TES array with its FDM-multiplexed SQUID readout; and c) a first demonstration of the mechanical integration of a large-format TES detector array and its 50 mK readout electronics.

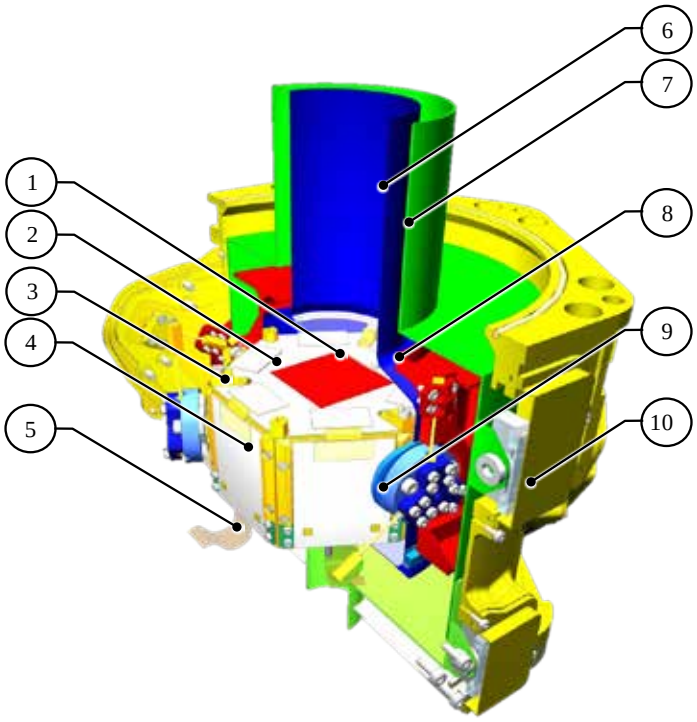

Fig. 2-1. *Conceptual design of a TES focal plane assembly for a far-IR imaging FTS spectrometer for SPICA-SAFARI. (1) TES array, (2) TES mount with hexagonal wafer on top, (3) supercondcuting flexible interconnect, (4) LC resonator unit, including LC filters and SQUID amplifiers, (5) 50mK to 2K cryo-harness, (6) Nb magnetic shield, (7) Cryoperm*

3 FPA magnetic shield design verification

3.1 Background

TES detectors and their SQUID amplifiers are extremely sensitive to magnetic fields, and magnetic shields are a key element in the FPA design in Fig. 2-1. Key requirements on these magnetic shields are to suppress the static field in the vicinity of the FPA to ~ 1 μT or less normal to the plane of the TES detector and temporal modulations in this field (e.g. linear drifts in the stray-field from an 50 mK ADR refrigerator and modulations in the stray-fields of compressors that drive mechanical cryo-coolers).

Previous work within an NL-funded activity led to the development of a design and prototype hardware for a two-layer magnetic shield to address these requirements (Fig. 3-1). A superconducting Niobium shield at 50 mK suppresses variability in the magnetic field environment by a factor of ~ 10^4. The Nb shield is surrounded by a mu-metal (Cryoperm) shield that suppresses the static external field by a factor of ~ 100 so that the Nb shield can be cooled in a low-field environment. This is needed because the field that is present during cooldown will be frozen into the Nb when it passes through its T_c, although the details of that process are non-trivial to model, as they depend upon the dynamics of the superconducting phase transition of the Nb.

The two-layer, two-material magnetic shield in Fig. 3-1 was developed using finite element models of isolated Cryoperm and Nb shields that were previously validated by measurements of simpler geometries. Within this activity, cryogenic measurements of a prototype two-layer magnetic shield were performed to verify its performance, and to validate finite element models of the integrated shield. Beyond this, a new test setup was developed to allow the magnetic field frozen into the Nb shield during cooldown to be measured, including tests of the dynamic behaviour of the Nb shield cooldown.

During the course of this work it was noted that the performance of some TES detector arrays may be optimized by applying a controlled, non-zero, uniform field perpendicular to the detector array to adjust the detector's operating point. Reflecting upon this new requirement, the setup used to characterize the field frozen into the Nb shield during cooldown was modified to include a coil to adjust the field level in the plane of the detector and to spatially map the field in the plane of the detector.

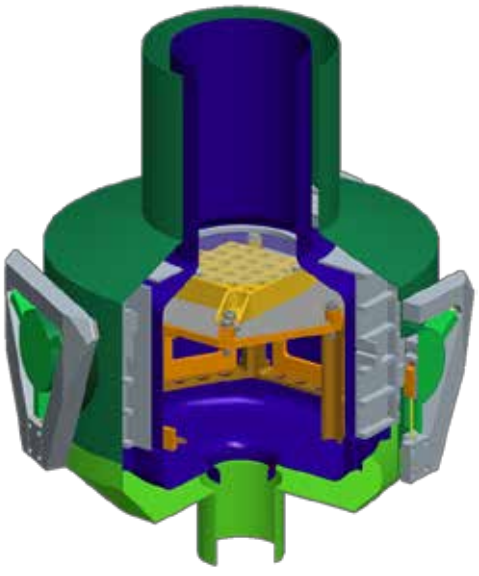

Fig. 3-1. *Preliminary FPA magnetic shield concept. A mu-metal Cryoperm shield (green) at 2 K suppresses the static external field, while a superconducting Nb shield (blue) at 50 mK provides a shielding factor of ~ 10^4 versus modulated fields. The achievable shielding is strongly dependent upon the shield geometry, in particular on the dimensions of the optical aperture. The Cryoperm shield reduces the field that is frozen in when the Nb passes through its superconducting transition temperature, ~ 9 K. The Nb shield is suspended inside the Cryoperm shield by a two-layer Kevlar suspension system and the detector assembly is located inside the Nb shield.*

3.2 Shielding factor verification

The prototype Cryoperm and Nb magnetic shields were tested at 4 K, first in isolation and then as an assembly, in order to verify finite element models of their shielding versus modulated external fields. These tests were performed at U. Twente, in collaboration with the EMS group of Prof. H.J.M. ter Brake, using an existing facility in which the shields could be cooled in a magnetically transparent cryostat. A three-axis SQUID magnetometer was used to measure the field inside the shields while varying the field environment in a magnetically shielded room, for fields parallel and perpendicular to the shield aperture. This measurement could also be performed with a controlled static field frozen into the Nb shield during its cooldown.

Fig. 3-2 shows a key result from TN 2.2 - the attenuation of a modulated external field parallel to the axis of the shield apertures, as a function of position along the axis of the shield. The measured attenuation for both an isolated Nb shield and the integrated Nb + Cryoperm shield agrees very well with finite element models. This result is true both when the shields are cooled down in zero external field, and when a static field is applied during cooldown. The good agreement between measurement and model provides confidence that the models can be used to predict the performance of optimized shield designs in the future.

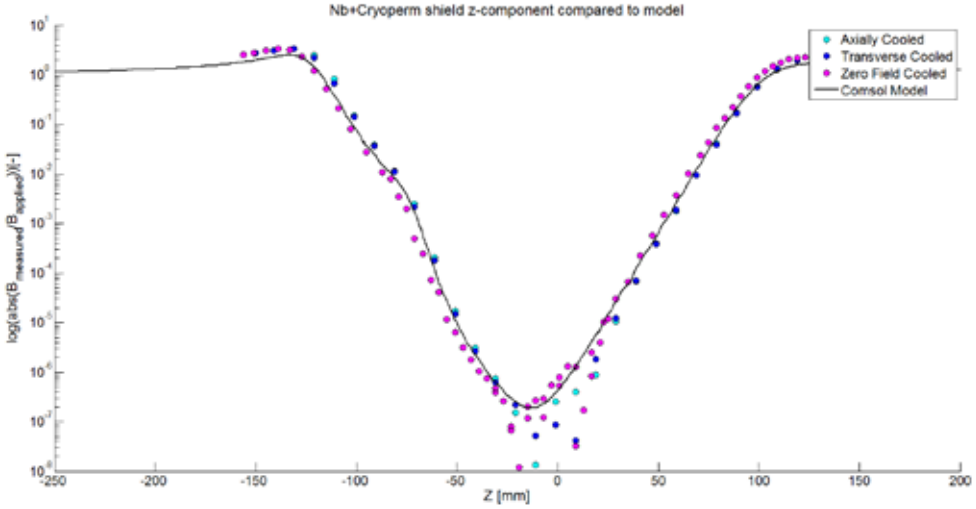

Fig. 3-2. *Measured on-axis shielding factor as a function of axial position within the shield vs. an axial external field for the integrated Cryoperm and Nb shield. The measurements were repeated for different frozen-in static fields, and the measured results agree very well with finite element (Comsol) models. The nominal detector position is at Z = 0 mm.*

3.3 Static field inside the Nb shield after cooldown

The next step in the shield verification was to adapt an SRON test cryostat to allow the static field frozen into the Nb shield to be measured for different field orientations (see TN 2.3). The integrated shield was mounted in an IR Labs LHe vacuum cryostat with the Cryoperm shield connected to the cryostat's 4 K cold stage. The Nb shield was suspended on a two-layer Kevlar suspension and a heat-switch was used to allow the Nb shield to be warmed up and then cooled down at a controlled rate through its T_c. Helmholtz coils outside the cryostat were used to control the magnetic environment during cooldown, and commercial flux-gate magnetometers were used to measure the magnetic field perpendicular to the detector. In this way, the field frozen into the Nb shield during cooldown could be measured as a function of both the external field orientation and the dynamics of the cooldown. A 2nd mechanical feedthrough was used to scan the position of the magnetometers, to sample the field along the optical axis and in the plane of the detector array.

Fig. 3-3 shows measured data for the field frozen into the Nb shield during a controlled, slow cooldown, representative of the cooling rate expected in an instrument. In this case, the measured field inside the Nb shield after cooldown is within 20% of the field measured just above the T_c of the Nb shield. The frozen-in field is thus roughly consistent with a model in which the external field, attenuated by the Cryoperm, is frozen into the Nb. Dynamic effects are seen to affect this result – previous tests at U.Twente showed that the frozen-in field can be reduced by a factor of ~ 2 if the cool-down is much faster, but that high cooling rates is not easily achieved in an instrument cooled by a space-qualified mechanical cooler. However, this result does show that the freezing of magnetic flux in the Nb shield is understood and can be modelled.

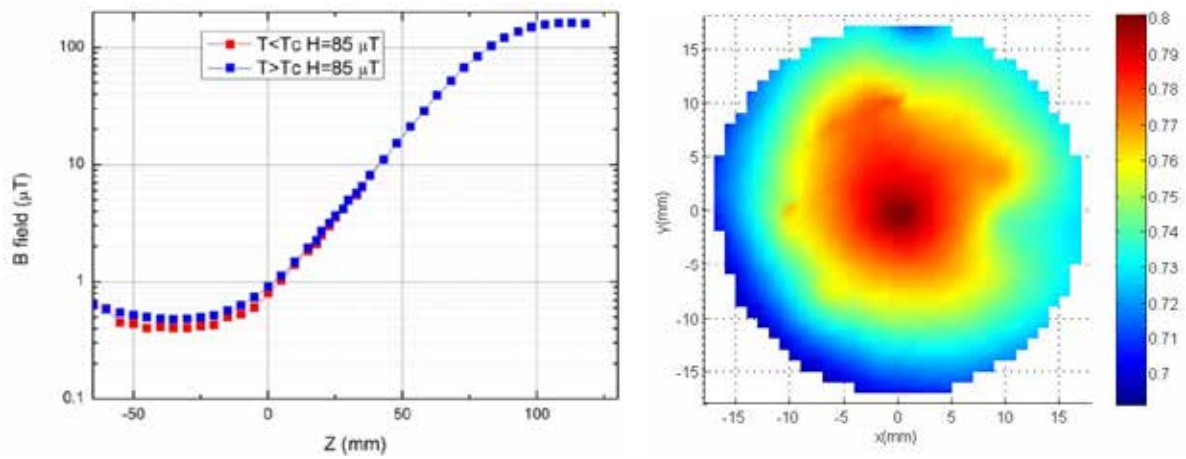

Fig. 3-3. *Measurement results for the magnetic field frozen into the integrated Nb + Cryoperm shield during cooldown. (left) When controlling the cooldown to an estimated rate for a space environment (0.05 K/min), the field after cooldown is within ~ 20% of the field present above T_c. (right) Sample magnetic field map over the detector plane for an external field of 85 μT. The colour scale is in μT.*

Fig. 3-3 also includes a map of the field perpendicular to the detector array, for an external field paralell to the optical axis, with B_{ext} = 85 μT. Similar measurements were performed for a range of field directions relative to the optical axis, $\alpha \in [0°, 22°, 45°, 90°, 135°, 158°, 180°]$. The maximum trapped field after cooldown varied from 0.2 to 0.8 μT as a function of the field direction, with a variation of less than 0.17 μT (p-p) within a circle with a radius of 18 mm from the central axis (the approximate size of TES bolometer array considered for SAFARI). This maximum variation was measured at α =135°. See TN 4.2 for more results.

3.4 Use of a field coil to define a controlled, non-zero field through the TES array

Beyond the requirement to suppress a static external field, it became clear during the contract it may also be desirable to tune the perpendicular magnetic field at the detector over +/- 5 μT, with good uniformity, to fine-tuning the operating point of the detector.

A potential solution to create such a magnetic bias is described in TN4.2. The superconducting shield close to the detector array obstructs the implementation of a Helmholtz coil, as the coil above the detector would be outside the shield. However, as there is no stringent requirement on the magnetic field in the plane of the detector, an alternative is generated with a single coil. Analytical expressions for a circular current loop with radius R show that the B_z component of a loop in the x-y plane is most uniform at a distance z= ½ R from this plane. To test this solution, a coil of radius R=30 mm to the test setup. For such a coil, the maximum predicted B_z component variation over a circle with a diameter of 24 mm at z= 15mm is < 1% peak.

4 TES-to-LC interconnect development

4.1 Interconnect concept

A critical element in the FPA design in Fig. 2-1 is an electrical interconnect between the TES and LC filter chips that: a) provides a low-resistance connection ($R \leq 1$ mΩ), b) allows the LC filter chips to be out of the plane of the TES chip for compact packaging, and c) is reworkable to facilitate testing and reworking.

A novel "coil-coupled" interconnect concept is considered to address these requirements (see Fig. 4-1), combining a superconducting flex circuit (for a low resistance "around-the-corner" connection) with bump-bonding to the LC filters and a reworkable transformer-coupled connection to the TES chip. Essential elements are superconducting flex circuits terminated on bulk Si (for coil patterning and bump-bonding), a reworkable interconnect-to-TES connection, and demonstration of a transformer-coupled TES. The first two points are addressed here. Fixed transformers are used to impedance-match TES and LC filters in the SRON FDM at SRON, while a transformer-coupled interconnect demonstration will follow the developments here.

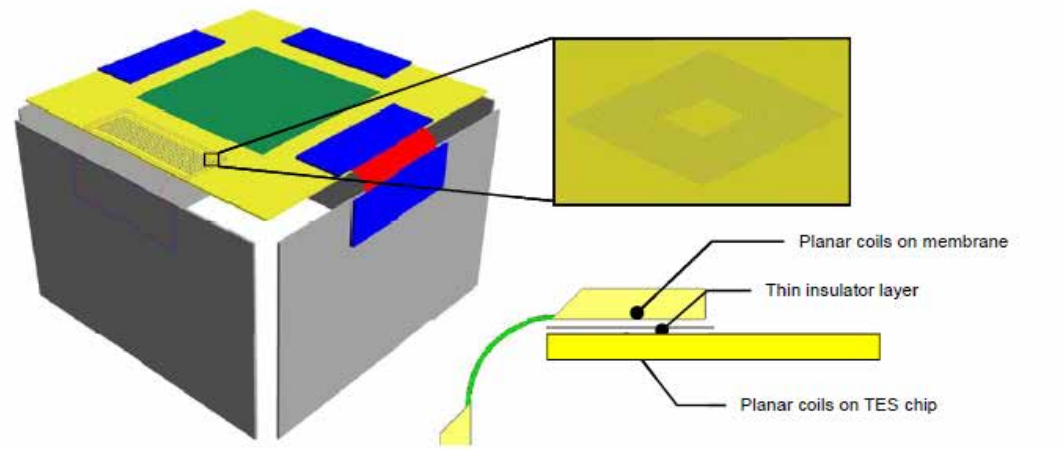

Fig. 4-1. *Left: Schematic view of a coil-coupled TES-to-LC interconnect. Right: The coil coupling transformer consists of planar coils (top right) on the TES chip and the bulk piece of the interconnect (blue). The signals pass around the corner using a Nb-on-Polyimide flex circuit (red). The connection to the LC filter chip (gray) can be bump-bonded.*

4.2 Superconducting flex circuit lithographic process development

The activities within this contract were intended to develop the building blocks of a coil-coupled interconnect, combine these in first prototype interconnect chips, and support the development of a mechanical concept for the interconnect and a prototype of the 50 mK detector and readout assembly. Considering the flex circuit development, 4 critical items were identified: a) a Nb-on-Polyimide-on-Si process, b) selective etching of Si to realize flex circuits with Si terminations, c) lithographically defined coils on one Si termination (contact to the TES chip), and d) a bump-bonded termination on the second Si termination (contact to the LC chip).

4.2.1 Nb-on-Polyimide flex circuits

Fig. 4-2 includes a schematic of the layer structure for Nb-on-Polyimide (PI) flex circuits with two-layer wiring and SiO_2 buffer layers between Ta/Nb/Ta wiring and PI layers. (see TN1.2, 1.3, and 1.6 for details). Initial Nb-on-PI-on-Si tests showed that Ta buffer layers in a Ta/Nb/Ta stack resulted in films with good superconducting properties. However, the superconducting transition temperature (T_c) of the Nb on PI was seen, likely due to stress in the Nb induced when the 2nd PI layer is cured. Despite this degradation, layers

with sufficiently high T_c were realized in Nb-on-flex circuits to allow testing at 4 K (see Fig. 4-2). Flex circuits were realized using wet and dry etching of bulk Si, with dry etching also allowing the definition of mechanical mounting features. Flex circuits with two-layer wiring were also demonstrated, using 250-nm SiO_2 between two Ta/Nb/Ta films to create a low-inductance wiring structure for high wiring densities (see TN1.3).

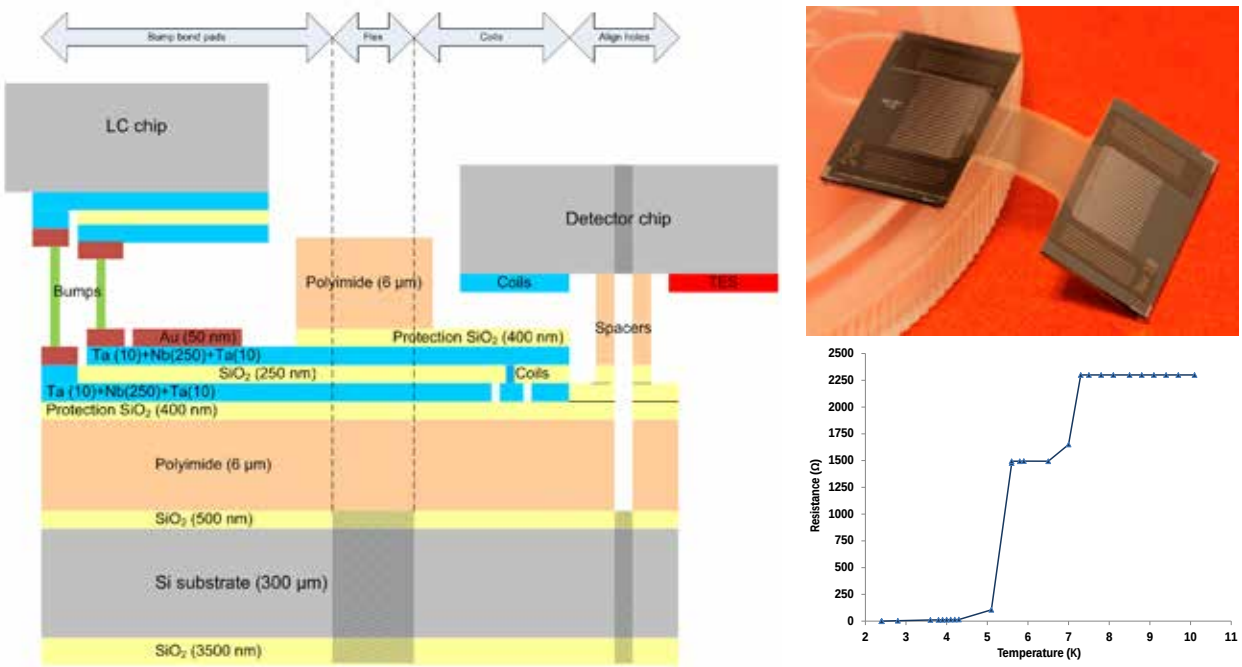

Fig. 4-2. *(left) Layer structure for Nb-on-Polyimide (PI) flex circuits with two-layer wiring and SiO2 buffer layers between the Ta/Nb/Ta wiring and PI layers. (top right) Prototype Nb-on-PI flex circuit. (bottom right) R-T measurement of a Nb-on-PI flex circuit, with two superconducting transitions attributed to Nb on the Si substrate and Nb in the flex circuit (lower T_c).*

NbTi was considered as an alternative to address the issue of T_c degradation, but no significant improvement was seen and Ta/Nb/Ta was used for most of this work. Test structures were introduced to the mask layouts used, allowing the resistance of sample Nb lines to be measured between process steps to track the layer properties and compare the properties of Nb on bulk Si and PI, also the upper and lower wiring layers.

4.2.2 Integration of coils in the Nb flex circuit process

A transformer-coupled interconnect-to-TES contact requires that lithographically defined coils are integrated in the Nb-on-flex process. A compact design is required to realize a compact connection, and coil designs similar to those in the SRON LC filter process were adopted, using 2-µm lines and spaces. Reliable coil patterning in the flex process was non-trivial, with patterning on the lower PI layer, step coverage at PI steps, and curing and patterning of the upper PI layer degrading the definition. These issues were partially addressed by flipping the standard SRON coil fabrication sequence (to fabricate the return line first, followed by the spiral) and adding SiO_2 layers between the Ta/Nb/Ta and PI layers, to stabilize the electrical properties and lithographic definition of the wiring, see Fig. 4-2 and TN1.6.

4.2.3 Realization of a bump-bond contact for the Interconnect-to-LC connection

The coil-coupled interconnect requires a high-density, low-impedance connection to the LC filters. This need not be reworkable, and bump-bonds are favoured over wire-bonds for high densities. Two materials were

considered: superconducting Indium and normal-conducting Au. Indium bumps are used at NIST to connect TES detectors and TDM readout circuits, driven by their low-impedance circuit and a need for "cold" bump-bonding to the TES chip. Because the transformer in the coil-coupled interconnect raises the TES impedance seen from the LC filter and LC filters can withstand higher temperatures, these constraints don't apply here, and we have chosen to apply a "standard" Au bump process.

This process was developed using a commercial flip chip aligner and Au stud placement at a commercial partner (QMicro), with sample fabrication and testiong at SRON. Superconducting structures connected by Au stud bumps yielded a bump contact resistance of ≤ 0.1 mΩ. However, the bumping force required for a large array (320 pairs) of stud bumps would be too large for the tool at QMicro. Thus, a new Au electro-plating process developed at SRON for x-ray microcalorimeter absorbers, was used to lithographically define Au bumps for bonding at QMicro, again yielding a bump resistance ≤ 0.1 mΩ. The bonding force required for an array of 640 lithographic bumps is feasible using the bonder at QMicro. See TN1.4 for more details.

4.2.4 Interconnect chip demonstration

The final step in development step within this contract was to combine the developed processes in prototype interconnect chips (see TN1.6 and Fig. 4-3). Several interconnect-LC combinations were realized:

- a mated LC filter and dummy bump-bond assembly for LC filter tests with bump-bonds in series,
- an LC-interconnect assembly for electrical tests, with a bump-bonded LC-interconnect connection and coupling coils at the open end of the flexible interconnect, and
- a prototype LC filter + flexible interconnect chip for integration in the prototype 50 mK assembly.

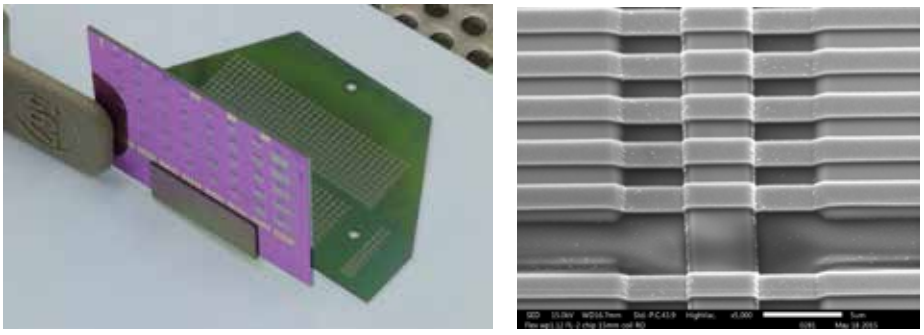

Fig. 4-3. Prototype interconnect chips. (left) LC filter chip bump-bonded to an interconnect chip. (right) SEM image of interconnect coil details. The steps where 2-µm wires pass over the return line are a likely location of excess low-temperature resistance in the coils.

The first demonstration showed that LC filters bump-bonded to a dummy chip have low series resistance at 4.2 K, and a series array of 160 bumps yielded a resistance 0.1 mΩ per bump, consistent with earlier predictions. Also, measurements of interconnect chips with coils showed that T_c > 6 K was realized in the both Nb layers in the interconnect chips, both on bulk Si and in the flex. However, these measurements also showed excess low-temperature resistance in the coils. The cause of this effect is still being investigated, but the narrowest Nb lines – the 2-µm lines in the coils are suspect. Inspection of the coils points to possible weak points in the steps over the coil return (see Fig. 4-3). Future actions to localize and address this issue are: a) optimize the return line patterning to realize less steep side-walls and reduce step-coverage issues, b) deposit the coils directly on the Si substrate, and c) consider the use of wider lines in the coils to reduce their susceptibility to step-coverage problems, at a cost of a larger footprint per coil.

5 Mechanical prototype of a 50 mK detector and readout electronics assembly

The final element of this activity was to develop a mechanical prototype of the 50 mK detector and readout assembly, starting with the development of a concept for a reworkable coil-coupled TES-to-LC interconnect.

5.1 TES-to-LC filter interconnect conceptual design and tolerance analysis

As a first step in the TES-to-LC filter interconnect design, a first mechanical concept was developed, with 6 trapezoidal interconnect terminations fixed to the TES wafer using three pins or screws each, as in Fig. 5-1. This concept was used to determine the TES wafer surface area available for electrical coupling and for preliminary mechanical analyses, e.g. of mechanical rigidity and alignment tolerances.

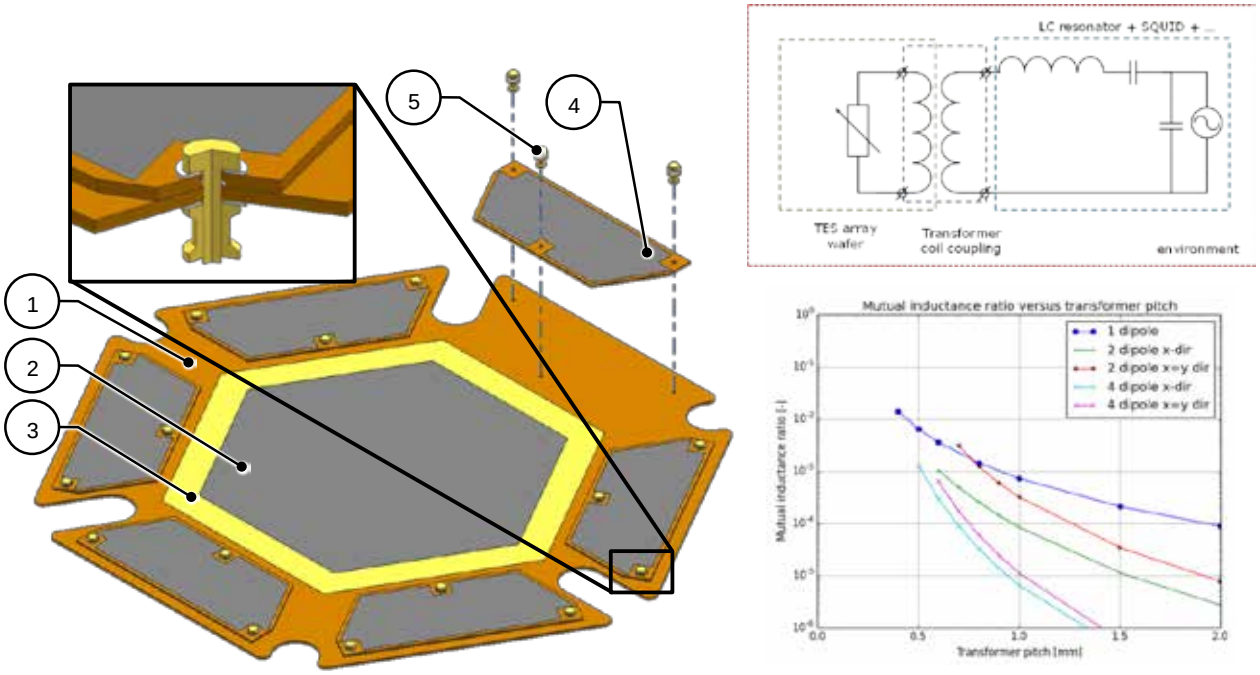

Fig. 5-1. *(left) First concept for transformer coupling to the TES wafer. Each TES pixel (2) is connected to a coil on the outer area of the wafer (1). The array and coil areas are separated by a thermalisation rim (3) plated on back side of the TES wafer (projected to the front here). The PI interconnect (not shown) between the TES and LC wafers ends in a Si section (4) with a secondary coil for each pixel. Each Si interconnect part is fixed to the TES wafer by 3 pins (5). (top right) Simplified coil coupling electrical schematic. (bottom right) Modelled mutual inductance between coils for single, dipole, and quadrupole coil designs.*

This concept also provided a framework for a first electrical design of the coil-coupling concept (see Fig. 5-1 and TN3.1), combining electromagnetic simulations of the coils and circuit simulations of the LC filter and TES to dimension and tolerance the system, including: dimensioning the coils; comparing single, dipole, and quadrupole coil designs; analyzing coil-to-coil cross-talk; and estimating the required mechanical tolerances.

5.2 Preliminary interconnect design and prototyping

This first design of a reworkable interconnect-to-TES connection was detailed, using precision pins to fix and align the TES and interconnect chips (see. Fig. 5-1 and 5-2) and dry-etched holes in Si to realize the required tolerances.

Prototypes of this design were produced to evaluate its feasibility (see TN3.2). Accurate alignment between dummy chips was realized. However, because dry-etched holes in Si have very sharp edges, contact forces between the pins and the Si were very high when the pins contacted the Si, chipping the edges (Fig. 5-3). Driven by concerns about damage to the detectors or optical filters by loose Si particles, it was decided that a extra (and unforeseen) design iteration was needed before proceeding with the 50 mK assembly.

The second design concept made use of precision-machined screws and nuts to fasten the Si chips (see Fig. 5-2 and TN3.3). Damage to the rims of the dry-etched holes in the Si is mitigated by gluing precision-machined metal inserts into the holes to limit metal-to-Si contact to the first assembly step (using a wafer probe station to insert the inserts with a minimum risk of damage to the TES wafer).

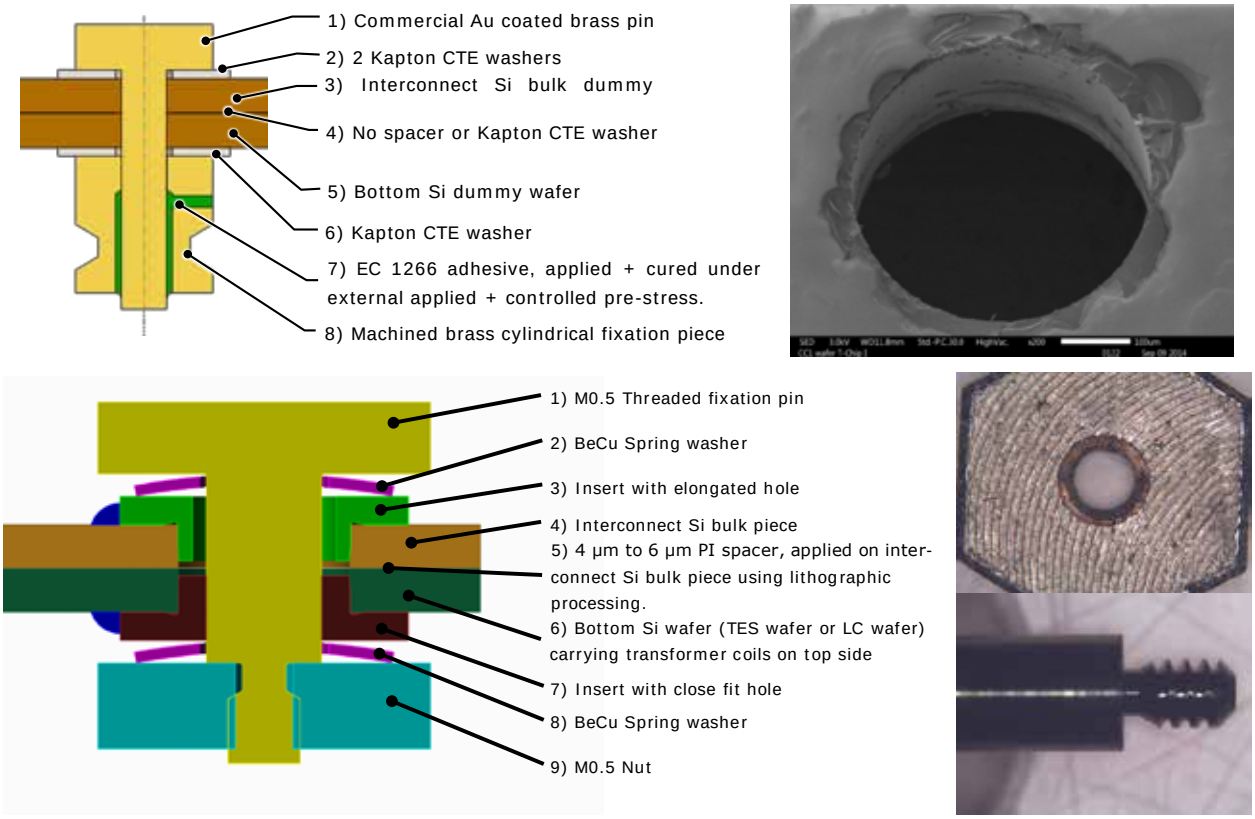

***Fig. 5-2**. (top) First interconnect fixation conccept. (top right) DRIE-etched hole in Si dummy chip after inserting and removing Au-coated brass pin using precision tooling. Contact stresses caused chippinng of the very sharp edges. (bottom) 2nd interconnect fixation concept using custom-made M0.5 screws and nuts and inserts glued into the Si chips to avoid damage to the chips (see right).*

5.3 50 mK detector and readout assembly mechanical prototype design

This new interconnect concept was applied in a mechanical prototype of the FPA's 50 mK detector and readout assembly (Fig. 5-3, TN3.3). The large TES and LC filter chips are mounted on arrays of leaf-springs wire-eroded into Cu support frames. The leaf springs absorb the CTE difference between Si and Cu and a symmetric configuration maintains the TES wafer alignment during cooldown (similar to the TES mount tested in the ESA-funded LTSA GSTP activity.) Structural analyses of the design were used to optimize its stiffness and strength, with a particular focus on the stiffness of the mounted TES wafer.

At the time that this design was developed, significant changes to the SAFARI concept were anticipated but implications the FPA were not known. As a result, it was decided to design this prototype to reflect the more stable X-IFU FPA concept (eg. TES and LC filter dimensions and with a dummy anti-coincidence detector assembly instead of horn and backshort arrays), to maximize the benefits to be gained from its realization.

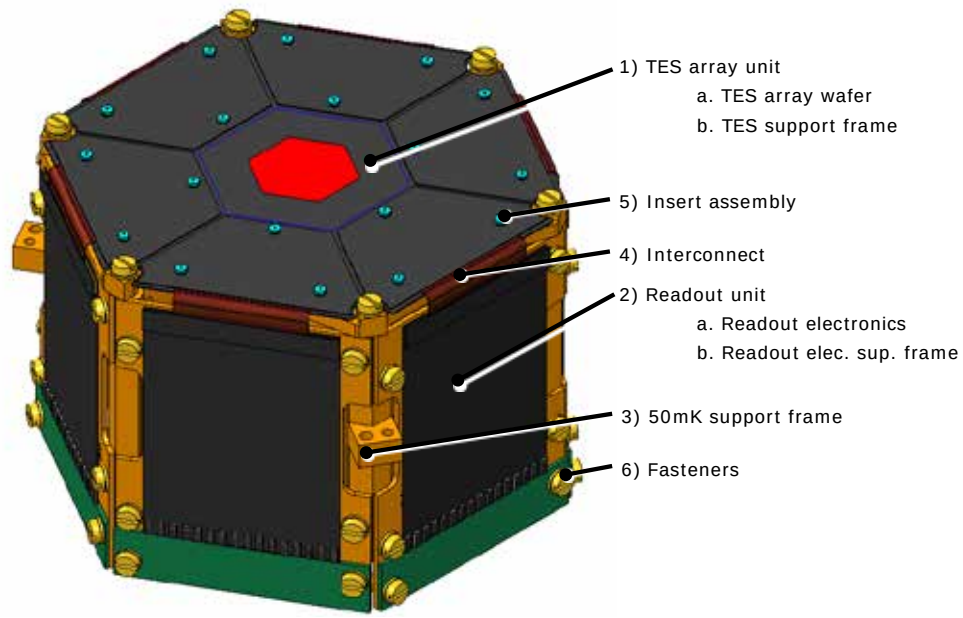

Fig. 5-3. *50 mK detector and readout assembly mechanical prototype.*

5.4 50 mK detector and readout assembly manufacturing and test results

A prototype 50 mK detector and readout assembly was developed (Fig. 5-4 and TN3.4) to verify its manufacturability and robustness vs. thermal cycling and random vibration. One prototype LC filter + flexible interconnect assembly was included, plus mass dummies for the remaining LC and interconnect chips. The TES chip is a structural dummy, including the silicon support grid for the TES pixels but no active pixels.

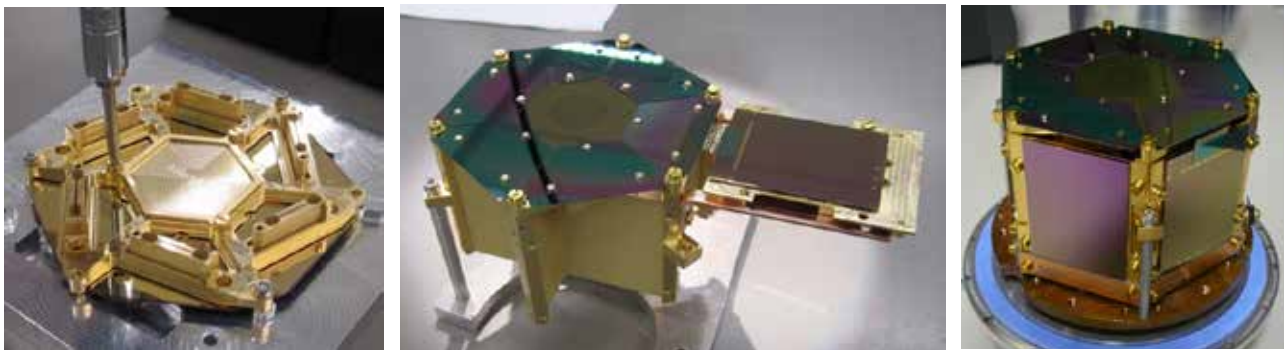

Fig. 5-4. *Prototype 50 mK detector and readout assembly: (left) integrating a CryoAC mass dummy on the TES mount, (middle) integrating the prototype LC + interconnect, (right) the final assembly.*

Once assembled the 50 mK mechanical prototype was thermally cycled 20 times to ~ 80 K, with no visual damage observed (see TN 4.3). Following the thermal cycle test, the assembly was vibration tested. Low-level sine sweeps were used to verify the assembly's stiffness and check integrity before and after vibration

tests. Random vibration tests were performed using spectra scaled in amplitude from preliminary estimates of qualification loads, starting at a low level and ramping up to the nominal test level (0dB). No damage was observed after the 0dB test, so testing continued to characterize the design's margins. The assembly survived a +3dB test, but the glue spots fixing the TES wafer to its support failed at +6dB.

Post-test disassembly and inspection confirmed a failure at the interface between the adhesive and the Cu support, and a detailed analysis of glued joints has started to understand this. Damage was also observed on the TES wafer under the corners of the interconnect chips, indicating that the interconnect chips made contact with the TES wafer during vibration. Related design modifications are considered for the future.

6 Conclusions and future work

This section summarizes the key conclusions of this activity. More details can be found in TN 5.2.

Considering the integrated Nb + Cryoperm magnetic shield, the measurements and analysis within this activity have significantly increased the maturity of the baseline design. Excellent agreement between experiment and models for the shielding vs. modulated fields has validated our FEM models below 10 Hz. Agreement between measurements and models of the flux trapped in the Nb shield during cooldown allow this effect to also be modelled, while first tests of using a coil to apply a magnetic field bias to the TES detector are promising. Points to be addressed in the future include: a) testing the Cryoperm shield at higher modulation frequencies, b) further developing the magnetic bias coil, and c) reviewing the instrument's shielding requirements. The B-shield drives the FPA's mass and volume. As such, realistic estimates of the detector susceptibility and FPA environment are needed to realize an optimized magnetic shield design.

Considering the TES-to-LC interconnect development, while good progress has been made and a multi-layer superconducting flex circuit has been developed, including compact two-layer wiring on the flex circuit and a Au bump-bond for the interconnect-to-LC connection, ongoing work is needed to pinpoint and resolve the root cause of the degradation of superconductivity in narrow Nb lines in the flexible interconnect process. Once this has been addressed, an important next step will be to electrically test a coil-coupled interconnect.

Reviewing the results of the prototype 50 mK detector and readout assembly, it is noted that a key design driver is the reworkable TES-to-LC interconnect. A mechanical concept for this connection has been developed, both in dummy chips and in a the 50 mK detector and readout assembly prototoype. The electrical design of this concept is still to be verified, including its mechanical tolerances and cross-talk estimates. The preliminary mechanical concept meets the estimated alignment requirements, and is robust vs. cryogenic thermal cycling and vibration. Further design optimization for assembly is desired, as is fine-tuning to address damage to the TES wafer due to contact with the interconnect chips during vibration. A FEM model is being developed to explain the adhesive failure in the TES wafer mount at high vibration levels (+ 6dB vs. the nominal test level). This model should be extended to model the effect thermal cycling, such that the adhesive bond can be optimized for both vibration loading and cryogenic thermal cycling.

In parallel with this activity, an alternative detector and readout assembly concept has been proposed, in which the LC filters and SQUIDs are moved to 300 mK. In this case, the first layer of the FPA's thermal suspension is part of the detector assembly, and the TES-to-LC interconnect flex circuit bridges 300 and 50 mK. This alternate concept has some thermal-mechanical advantages (e.g. lower mass at 50 mK), and a detailed comparison is ongoing. Future work on the 50 mK assembly should also incorporate a prototype cryogenic anti-coincidence detector (for an x-ray FPA) or horn and backshort arrays (for a far-IR FPA).